Raman Microspectrometry Study of Electrochemical Lithium Intercalation into Sputtered Crystalline V_2O_5 Thin Films

R. Baddour-Hadjean,*,† J. P. Pereira-Ramos,† C. Navone,† and M. Smirnov‡

Institut de Chimie et Matériaux Paris-Est, Unité Mixte de Recherche (UMR) 7182 Centre National de la Recherche Scientifique (CNRS) et Université Paris XII, GESMAT, 2 rue Henri Dunant 94320 Thiais, France, Fock Institute of Physics, St. Petersburg State University, 198504 - St. Petersburg, Russia

Received October 16, 2007. Revised Manuscript Received December 7, 2007

Raman microspectrometry has been used to investigate the local structural changes induced by the electrochemical lithium intercalation reaction in crystalline sputtered V_2O_5 thin films in a liquid electrolyte. Contrary to usual composite electrodes made of a mixture of active material and conductive and binding agents, the use of a pure V_2O_5 thin film allows a homogeneous Li insertion in the material and a high quality of Raman signatures to be obtained. The Raman spectra of $Li_xV_2O_5$ compounds for $0 < x < 1$ are examined as a function of the lithium content and discussed in relation with the X-ray diffraction data pertinent to these *h00*-oriented thin films and literature data. An assignment of all Raman bands is proposed, and the Raman fingerprint of the ϵ-type phase, whose interlayer distance continuously increases with x, is clearly evidenced all along the Li insertion process: lithium ions rapidly produce an orthorhombic ϵ phase characterized by a vanadyl stretching mode at 984 cm^{-1} for $0 < x < 0.5$, and further Li accommodation induces a splitting into two stretching modes, the first one shifting from 984 to 975 cm^{-1}, the second from $x = 0.7$ located at a fixed wavenumber of 957 cm^{-1}. Both modes are consistent with the local structure of the ϵ lithium-rich phase called ϵ' and reflect the existence of two different lithium sites. This work illustrates that the structural changes, in terms of long-range order and local structure, are strongly dependent on the microstructure and morphology of the material.

Introduction

There is growing interest in producing lithium batteries in the form of thin-film devices for many applications such as on-chip power sources, smartcards, and portable electronic equipment. Therefore, many thin-film cathode materials; transition metal sulfides; oxysulfides and oxides including $LiCoO_2$, $LiMn_2O_4$, and partially substituted Co and Mn derivatives of $LiNiO_2$; and V_2O_5 have been extensively investigated. Due to its large specific capacity (theoretical value: 440 mA h/g) in the potential range 3.8/1.5 V[1–7] and a post annealing treatment, when required, at moderate temperatures (<300 °C), vanadium pentoxide film is considered to be an interesting candidate.

As for bulk oxides in composite electrodes, the electrochemical properties of pure thin films are strongly dependent on the structural changes induced by the lithium insertion reaction. Several studies carried out on polycrystalline films seem to show that the structural features of the lithiated $Li_xV_2O_5$ phases can be significantly different from that known for the bulk material.[8–13] *In situ* and *ex situ* X-ray diffraction (XRD) experiments performed on sol–gel and sputtered $Li_xV_2O_5$ films have shown the existence of an unexpected elongated *c* axis for $x = 0.8$ as well as the nonappearance of the δ phase usually described for $x = 1$ in bulk samples.[8,9,12,13] We have recently reported the attractive electrochemical properties of crystallized oriented V_2O_5 films prepared either by direct current or radio frequency (rf) magnetron reactive sputtering without any heat treatment.[14,15] Once again, a different structural response of the thin-film electrode was observed from X-ray diffraction experiments when Li insertion proceeded in V_2O_5 ($0 < x < 1$ for x in $Li_xV_2O_5$) since the emergence of the δ phase does not seem to take place as in the bulk material from $x = 0.6$.[16]

* Author to whom correspondence should be addressed. E-mail address: baddour@glvt-cnrs.fr.
† UMR 7182 CNRS et Université Paris XII.
‡ St. Petersburg State University.

(1) Bates, J. B.; Dudney, N. J.; Lubben, D. C.; Gruzalski, G. R.; Kwak, B. S.; Yu, X.; Zuhr, R. A. *J. Power Sources* **1995**, *54*, 58.
(2) Zhang, J. G.; McGraw, J. M.; Turner, J.; Ginley, D. *J. Electrochem. Soc.* **1997**, *144*, 1630.
(3) Park, Y. J.; Ryu, K. S.; Kim, K. M.; Park, N. G.; Kang, M. G.; Chang, S. H. *Solid State Ionics* **2002**, *154*, 229.
(4) Park, Y. J.; Ryu, K. S.; Park, N. G.; Hong, Y. S.; Chang, S. H. *J. Electrochem. Soc.* **2002**, *149*, A597.
(5) Kumagai, N.; Kitamoto, H.; Baba, M.; Durand-Vidal, S.; Devilliers, D.; Groult, H. *J. Appl. Electrochem.* **1998**, *28*, 41.
(6) Kumagai, N.; Komaba, S.; Nakano, O.; Baba, M.; Groult, H.; Devilliers, D. *Electrochemistry* **2004**, *72*, 261.
(7) West, K.; Zachau-Christiansen, B.; Skaarup, S. V.; Poulsen, F. W. *Solid State Ionics* **1992**, *57*, 41.
(8) Talledo, A.; Granqvist, C. G. *J. Appl. Phys.* **1995**, *77*, 4655.
(9) Scarminio, J.; Talledo, A.; Andersson, A. A.; Passerini, S.; Decker, F. *Electrochim. Acta* **1993**, *38*, 1637.
(10) Ptitsyn, M. V.; Tikhonov, K. I.; Rotinyan, A. L. *Sov. Electrochem.* **1981**, *17*, 1297.
(11) Andrukaitis, E.; Jacobs, P. W. M.; Lorimer, J. W. *Solid State Ionics* **1988**, *27*, 19.
(12) Meulenkamp, E. A.; Van Klinken, W.; Schlatmann, A. R. *Solid State Ionics* **1999**, *126*, 235.
(13) Vivier, V.; Farçy, J.; Pereira-Ramos, J. P. *Electrochim. Acta* **1998**, *44*, 831.
(14) Navone, C.; Pereira-Ramos, J. P.; Baddour-Hadjean, R.; Salot, R. *J. Electrochem. Soc.* **2006**, *12*, 153.
(15) Navone, C.; Baddour-Hadjean, R; Pereira-Ramos, J. P.; Salot, R. *J. Electrochem. Soc.* **2005**, *152*, 1790.
(16) Cocciantelli, J. M.; Doumerc, J. P.; Pouchard, M.; Broussely, M.; Labat, L. *J. Power Sources* **1991**, *34*, 103.

10.1021/cm702979k CCC: $40.75
Published on Web 02/19/2008

This specific behavior reported for polycrystalline V_2O_5 films requires deeper structural investigations, and for this purpose, Raman spectroscopy is very appropriate as it constitutes a very sensitive tool to detect local structural variations. Some researchers have used Raman spectroscopy to characterize powdered $Li_xV_2O_5$ phases.[17–20] Nevertheless, little relevant information can be extracted. An *ex situ* study has focused on the δ-, ϵ- and γ-$Li_{0.95}V_2O_5$ compounds[17] for which in fact only the γ Raman spectrum can be considered, the other spectra corresponding to degradation compounds locally produced under the laser beam. Moreover, *in situ* experiments exhibit serious limitations due either to the fluorescence of the electrolyte[19] or to the high Raman activity of the organic solvent, which prevents the observation of the V_2O_5 typical vibrational modes in the high-frequency range.[20] On the other hand, spectroscopic investigations of Li-intercalated V_2O_5 polycrystalline films have also been carried out.[21–24] However, reported data are very scarce and controversial due to the fact that the efficiency of Raman spectroscopy depends on the availability of a relevant band assignment. Moreover, most of these studies suffer from the lack of complementary XRD data, which prevents the identification of the lithiated phases and any relevant structural discussion. Some of us have recently reported, for the first time, the reference Raman spectra of the ϵ-$Li_{0.5}V_2O_5$, δ-LiV_2O_5, and γ-LiV_2O_5 powdered phases chemically prepared and have evidenced the great metastability of the δ phase under the laser beam, which has allowed a review of some literature data.[25] In the present paper, we afford a new perspective in the study of the structural changes occurring in the V_2O_5 film under operation by performing a Raman microspectrometry investigation of discharged and charged $Li_xV_2O_5$ thin-film electrodes as a function of the Li content x for $0 \leq x \leq 1$.

Experimental Section

Vanadium oxide films were deposited in an Alcatel SCM 600 apparatus on a stainless steel substrate (100-μm-thick foils) by rf magnetron reactive sputtering using a vanadium metal target (99.7%) of 150 mm diameter according to experimental conditions described in ref 14. The film thickness (600 nm) was controlled by deposition time and measured by a profilometer. The mass deposit of the film was obtained by weighing measurements and chemical analysis using inductively coupled plasma−atomic emission spectrometry experiments.

The surface morphology of the deposited films was investigated by scanning electron microscopy (SEM) using a LEO 1530SEG apparatus.

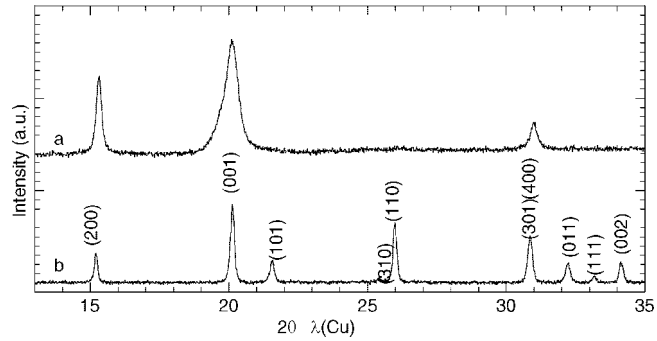

Figure 1. XRD patterns of (a) c-V_2O_5 600-nm-thick film deposited on a nickel substrate by rf magnetron reactive sputtering and (b) V_2O_5 powder.

XRD data were collected using a Brucker D8 Advance diffractometer with Cu Kα radiation ($\lambda_{K\alpha} = 1.5406$ Å) over a scanning angle 2Θ range of 10–50° at a scan rate of 0.015°/s.

The Raman spectra were recorded at room temperature using a LaBRAM "Infinity" (Jobin-Yvon-Horiba) Raman microspectrometer including Notch filters and equipped for signal detection with a back-illuminated charge-coupled device detector (Spex CCD) cooled by the Peltier effect to 200 K. A Nd:YAG laser (532 nm) was used as the excitation source. The spectra were measured in back-scattering geometry. The resolution was about 0.5 cm^{-1}. A 100× objective was used to focus the laser light on the sample surface to a spot size of 1 μm^2. To avoid local heating of the sample, the power of the laser beam was adjusted to 0.2–0.5 mW with neutral filters of various optical densities. The deconvolution of Raman spectra has been performed using the laboratory-produced "PAMIR" software.

The working composition of the oxide thin film was changed by coulometric titration using a *C*/20 rate in two-electrode cells (Swagelok type). Equilibrium was considered to be reached when the open circuit voltage remained stable (<2 mV for 24 h). The electrochemical cell was prepared inside a dry box by placing a clean lithium metal disk (13 mm diameter), a glass fiber separator soaked with the electrolyte solution (1 mol L^{-1} of $LiClO_4$, dried under a vacuum at 180 °C for 15 h and dissolved in twice-distilled propylene carbonate obtained from Fluka), and the cathode film (0.5 cm^2) into a Teflon container with two stainless steel terminals.

Results and Discussion

X-ray Diffraction and SEM Microscopy. As shown in Figure 1, the X-ray diffraction pattern for the V_2O_5 thin film is typical of a well-crystallized sample. It exhibits only three typical diffraction lines, (200), (001), and (400)(301) of the orthorhombic V_2O_5 phase, space group *Pmmn*, with lattice parameters a and c of the orthorhombic cell equal to 11.50 and 4.40 Å, respectively.

The SEM micrograph (Figure 2) reveals that the V_2O_5 thin film is viewed as standing platelets perpendicular to the surface and from which the thin cross section, on the order of 20 nm, can be observed. This specific morphology is in good accord with XRD data indicating an *h00* preferred orientation (Figure 1) and a high porosity.[14,15] The films have preferentially grown along the a direction perpendicular to the substrate, and the stacking of the *ab* planes is probably performed at a short distance corresponding to the thickness of the platelets, which never exceeds 10–20 nm in the c direction.

(17) Zhang, X.; Frech, R. *Electrochim. Acta* **1997**, *42*, 475.
(18) Zhang, X.; Frech, R. *J. Electrochem. Soc.* **1998**, *145*, 847.
(19) Rey, I.; Lassègues, J. C.; Baudry, P.; Majastre, H. *Electrochim. Acta* **1998**, *43*, 1539.
(20) Burba, M.; Frech, R. *Appl. Spectrosc.* **2006**, *60*, 490.
(21) Cazzanelli, E.; Mariotto, G.; Passerini, S.; Decker, F. *Solid State Ionics* **1994**, *70/71*, 412.
(22) Baddour-Hadjean, R.; Golabkan, V.; Pereira-Ramos, J. P.; Mantoux, A.; Lincot, D. *J. Raman Spectrosc.* **2002**, *33*, 631.
(23) Ramana, C. V.; Smith, R. J.; Hussain, O. M.; Massot, M.; Julien, C. M. *Surf. Interface Anal.* **2005**, *37*, 406.
(24) Julien, C.; Ivanov, I.; Gorenstein, A. *Mater. Sci. Eng., B* **1995**, *33*, 168.
(25) Baddour-Hadjean, R.; Rackelboom, E.; Pereira-Ramos, J. P. *Chem. Mater.* **2006**, *18*, 3548.

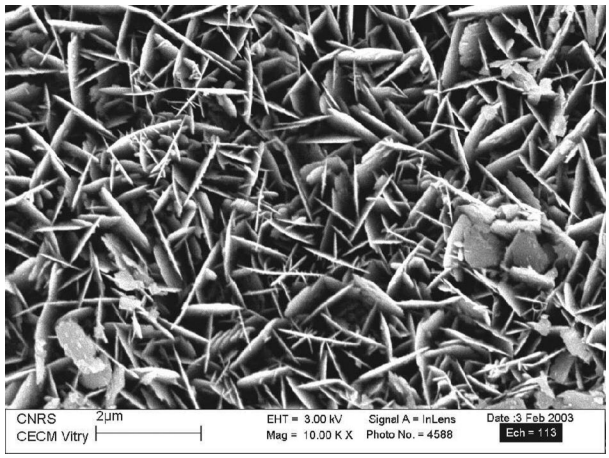

Figure 2. SEM micrograph of a 600 nm V_2O_5 thin film.

Raman Spectroscopic Analysis of Pure V_2O_5 Thin Films. The point symmetry group of V_2O_5 is D_{2h}. The structure of the vanadium−oxygen layers in V_2O_5 is presented in Figure 3. It can be seen (Figure 3c) that the vanadium atom is located within the oxygen coordination polyhedron, VO5, and is shifted toward the plane formed by four oxygen atoms by a distance of 0.47 Å. Four types of V−O bonds, characterized by their particular bond length, can be distinguished:

- The short and strong apical V═O_1 bonds, d_1 = 1.577 Å.
- The bridge V−O_3 bonds, d_2 = 1.779 Å.
- The "ladder step" V−O_2 bonds (giving to two equivalent intraladder V−O_{21} and V−O_{22} bonds), d_3= 1.878 Å.
- The interchain V−O_2 bonds (labeled as V−$O_{2'1}$ in Figure 3c), d_4= 2.017 Å.

Polarized Raman[26] and IR reflection[27] spectra of the V_2O_5 crystal have been thoroughly studied and interpreted on the basis of the phonon state calculations.

A qualitative characterization of the normal vibrations of the V_2O_5 lattice can also be done in terms of atomic displacement. With all valence V−O bonds being oriented along coordinate axes (see Figures 3a and b), any bond-stretching mode involves oscillations of particular oxygen atoms along particular Cartesians axes. Moreover, due to the difference in bond lengths, the spectral lines characteristic for the bond-stretching oscillations of the different V−O bonds can be easily selected.

There are four symmetry-equivalent atomic positions per unit cell for the V, O_1, and O_2 atoms and only two for the O_3 atoms, because they lie in the mirror plane perpendicular to the x axis. All of these positions correspond to atoms of the same layer, and all layers, which alternate with each other in the z direction, are equivalent. By using the standard table of characters of irreducible representations of the D_{2h} group, 12 symmetric combinations can be built from Cartesian displacements of four equivalent atoms, six of which are IR-active, and six others are Raman-active. The Raman-active combinations are shown in Figure 4, numbers 1, 2, 3, and 4 referring to the four symmetry-equivalent atomic positions for a given atom in the unit cell. It is seen that the x and z displacements give rise to A_g and B_{2g} modes, while the y displacements give rise to B_{1g} and B_{3g} modes. Taking also into account the infrared B_{1u} and B_{3u} IR-active modes related to x and z displacements, respectively, and the A_u and B_{2u} species related to $y$displacements, the vibrational species for V, O_1, and O_2 atomic motions can be represented as

$$\Gamma(\mathrm{V}) = \Gamma(\mathrm{O}_1) = \Gamma(\mathrm{O}_2) = 2A_g + 2B_{2g} + B_{1g} + B_{3g} + 2B_{1u} + 2B_{3u} + A_u + B_{2u}$$

Due to the special position of the O_3 atoms, the $x(O_3)$ displacements do not contribute to A_g and B_{1u} modes, the $z(O_3)$ displacements do not contribute to B_{2g} and B_{3u} modes, and the $y(O_3)$ displacements do not contribute to B_{1g} and A_u modes. Hence, the vibrational species for the motion of this atom can be expressed as

$$\Gamma(\mathrm{O}_3) = A_g + B_{2g} + B_{3g} + B_{1u} + B_{3u} + B_{2u}$$

In total, the optically vibrational modes of V_2O_5 are obtained from the overall contributions of each atom after subtracting the acoustic modes ($\Gamma_{\mathrm{acoustic}} = B_{1u} + B_{2u} + B_{3u}$).

$$\Gamma(\mathrm{V_2O_5}) = \sum \Gamma(\mathrm{i}) - \Gamma_{\mathrm{acoustic}} = [7A_g + 7B_{2g} + 3B_{1g} + 4B_{3g} + 7B_{1u} + 7B_{3u} + 3A_u + 4B_{2u}] - [B_{1u}(\mathrm{ir}) + B_{2u}(\mathrm{ir}) + B_{3u}(\mathrm{ir})]$$

$$\Gamma(\mathrm{V_2O_5}) = 7A_g + 7B_{2g} + 3B_{1g} + 4B_{3g} + 6B_{1u} + 6B_{3u} + 3A_u + 3B_{2u}$$

We expect, therefore, 21 modes in the Raman spectrum of V_2O_5.

The Raman spectrum of the pure sputtered V_2O_5 film is shown in Figure 5. The frequency distribution of the normal vibrations of V_2O_5, with their assignments to particular atomic displacements, is presented in Table 1. The modes originated from the same atomic displacement are gathered in the rows of Table 1. The modes of different symmetry are arranged in different columns of this table. It is seen that the modes involving the same atomic displacements have rather close wavenumbers.

The bond stretching modes cover the interval of 500–1000 cm^{-1}. First, z displacements of O_1 atoms give rise to the highest-frequency $\nu(d_1)$ mode at 994 cm^{-1}. It corresponds to the in-phase stretching vibration of all apical V−O_1 bonds. The Raman-active $\nu(d_1)$ mode of B_{2g} symmetry expected around 976 cm^{-1} was not detected in our spectra. The low intensity of this mode is quite comprehensible. According to the general theory of Raman intensities,[28] the main contributions to the Raman tensor for the bond stretching modes are determined by derivatives of bond polarizability with respect to the bond lengths. Owing to symmetry of the B_{2g} representation, half of the V−O_1 bonds stretch, whereas the other half shorten. So, this mode is permitted for Raman spectra by symmetry but is inactive, owing to its particular microscopic pattern. In ref 26, this mode was assigned to a very weak Raman peak observed at 976 cm^{-1}.

Next in the frequency scale is the $\nu(d_2)$ mode which comes from $x(O_3)$ displacements and which corresponds to an

(26) Abello, L.; Husson, E.; Repelin, E.; Lucazeau, G. *Spectrochim. Acta, Part A* **1983**, *39*, 641.
(27) Clauws, P.; Vennik, J. *Phys. Status Solidi B* **1980**, *59*, 469.
(28) Zerbi, G. *Vibrational intensities in infrared and Raman spectroscopy*; North Holland Publishing Co.: Amsterdam, 1982; p 23.

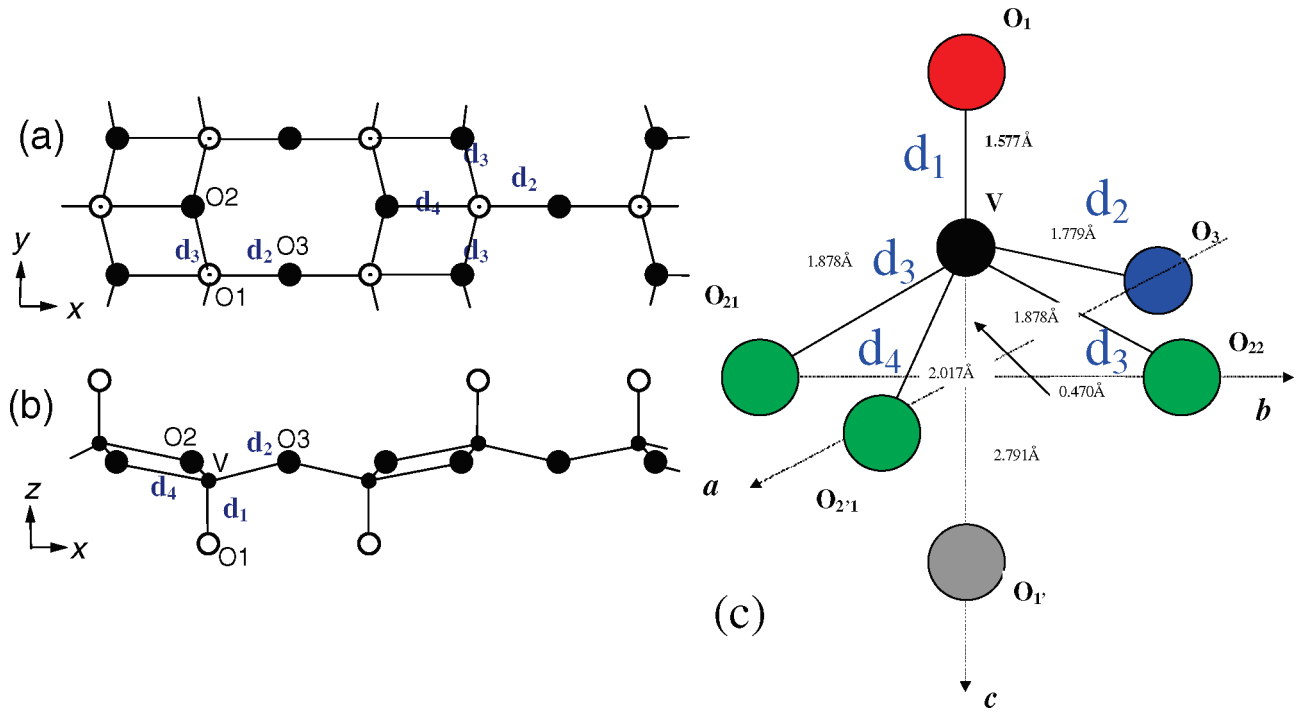

Figure 3. Crystal structure of V_2O_5 in *xy* (a), *xz*-projection (b), and local vanadium environments (c). The V atoms are shown by small black circles, and the O_2 and O_3 atoms are shown by large black circles. The O_1 atoms are shown by large open circles.

antiphase stretching of the V−O_3 bonds forming the V−O_3−V bridges. This mode of B_{2g} symmetry, calculated at 848 cm^{-1},[26] was also not detected experimentally. The low Raman intensity of this mode is caused by the fact that the V−O_3−V bridge is pseudocentrosymmetric (the V−O_3−V angle is 148°).

Then follows the $\nu(d_3)$ mode (at 700 cm^{-1}) involving the $y(O_2)$ displacements. It corresponds to an antiphase stretching of the V−O_2 bonds. The V−O_2 bonds (1.88 Å) are longer than the V−O_3 bonds (1.78 Å). Correspondingly, frequencies of the O_2 modes are lower than that of the O_3 mode.

The Raman-active mode at around 526 cm^{-1} originates from the $\nu(d_4)$ stretching vibration involving *x* displacements of $O_{2'}$ atoms. The A_g mode gives rise to the Raman line observed at 526 cm^{-1}. The B_{2g} line at 502 $cm^{-1}$was not detected because of its low intensity.

The angle bending modes cover the interval of 200–500 cm^{-1}. It is more difficult to determine the frequency distribution for these modes because of considerable coupling. The Raman peak at 480 cm^{-1} can be characterized as bending vibrations of the V−O_3−V bridge angle (see Figure 3).

Raman bands in the frequency region between 400 and 200 cm^{-1} correspond to the modes which involve the *x* and *y* displacements of O_1 atoms at 403 and 282 cm^{-1}, respectively, and *z* displacements of O_{21} and O_{22} atoms at 302 cm^{-1}. These atomic displacements produce the $\delta(O_1-V-O_2)$ and $\delta(O_1-V-O_3)$ bending deformations. Corresponding modes can be characterized as the V−O_1 bond rocking oscillations. The V−O_1 rocking in the *xz* plane, which involves the O_1 atoms oscillations along the *x* axis, gives rise to the A_g Raman peak at 403 cm^{-1}. The Raman features at around 300 cm^{-1} correspond to the modes involving *y* oscillations of O_1 atoms accompanied with *z* oscillations of O_2 atoms. Two peaks in the low-frequency region are associated with the modes involving displacements of the V atoms. The line at 195 cm^{-1} comes from A_g and B_{2g} modes, with the atoms oscillating along the *x* axis. The most intense Raman line at 144 cm^{-1} corresponds to a mixture of signals coming from B_{1g} and B_{3g}. The B_{1g} mode involves the shear motion of the ladders, whereas the B_{2g} consists of rotations of the ladders along their axes. The high intensity of this line reflects the long-range order in the plane of the vanadium oxygen layers.

Raman Spectroscopic Analysis of the Electrochemically Lithiated $Li_xV_2O_5$ Thin Film. The galvanostatic discharge–charge curves of the 600-nm-thick film are reported in Figure 6 at different *C* rates between 3.8 and 2.8 V. Two well-defined insertion steps located at about 3.4 and 3.2 V are observed, as expected for the crystalline form of V_2O_5, according to the following equation:

$$V_2O_5 + xLi^+ + xe^- \leftrightarrow Li_xV_2O_5 \qquad (1)$$

The specific capacity obtained at a rate of *C*/15 is 22 μAh/cm^2, which corresponds to the accommodation of 0.94 Li^+ ions per mole of oxide. This insertion reaction is reversible, as shown from the lack of polarization and the efficiency of 100% in the charge process. No influence of the current density on the discharge potential and capacity is seen from *C*/15 up to a *C*/5 rate, and the specific capacity is seen to decrease by only ≈18% when the *C* rate increases from *C*/15 to 8*C*. Moreover, the polarization observed at high rates never exceeds 150 mV, which suggests a high level of kinetics of lithium transport.

It is of interest to examine the evolution of the structural response of the *h00*-oriented V_2O_5 film as lithium accommodation proceeds, and for that, both XRD and Raman

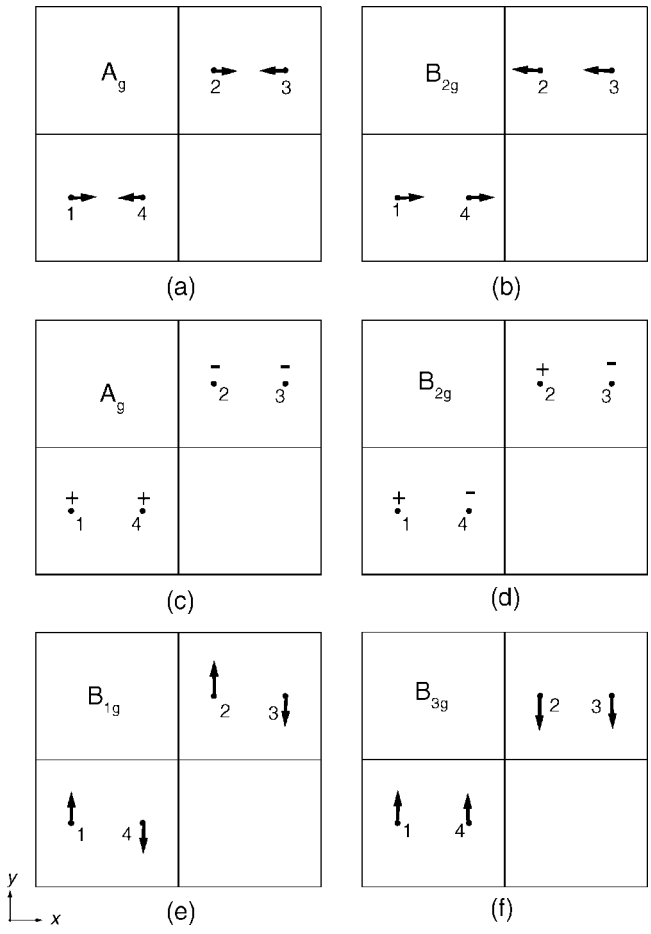

Figure 4. Symmetric atomic displacement combinations for the *Pmnn* space group.

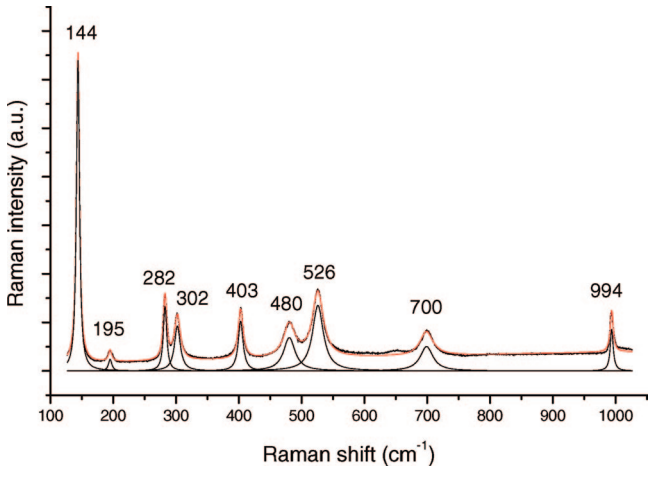

Figure 5. Raman spectrum of the V_2O_5 thin film, with the deconvolution of the different bands shown below.

microspectrometry have been applied. XRD experiments have been published elsewhere,[15] and present spectroscopic data will be discussed in light of these results. Figures 7 and 8 pertain to Raman spectra with different x values in $Li_xV_2O_5$ thin films.

Examining the Raman spectra collected in the $0 < x < 0.5$ composition range (see Figure 7), several observations can be made. First, the intensity of the translational mode at low frequencies is progressively quenched, and its wavenumber is shifted from 144 to 156 cm^{-1} for $x = 0.5$. Several

Table 1. Symmetry and Frequency Distribution (cm^{-1}) of Normal Vibrations of the V_2O_5 Lattice with Their Assignment to Particular Atomic Displacements

atomic displacement	assignment	A_g	B_{2g}
Z(O1)	$\nu(d_1)$	994	976[a]
X(O3)	$\nu(d_2)$		848[a]
X(O2′)	$\nu(d_4)$	526	502[a]
Z(O3)	δ(V−O3−V)	480	
X(O1)	ρ(V═O1)	403	350[a]
Z(O2)		302	310[a]
X(V)	δ(O2−V−O2)	195	195
Z(V)	δ(O3−V−O2)	104	143[a]

atomic displacement	assignment	B_{1g}	B_{3g}
Y(O2)	$\nu(d_3)$	700	700
Y(O1)	ρ(V═O1)	282	282
Y(O3)	δ(O2−V−O2)		220[a]
Y(V)	δ(O3−V−O2)	144	144

[a] Not observed experimentally.

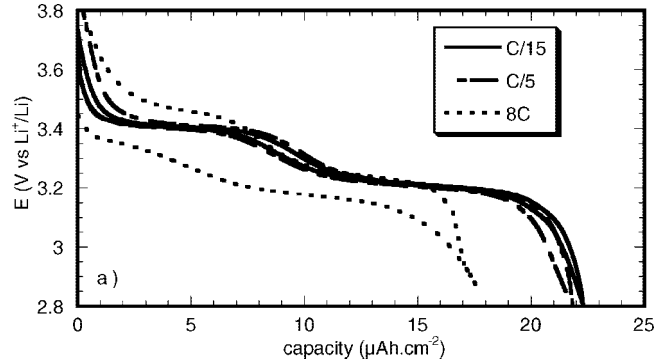

Figure 6. The first discharge–charge cycles of a V_2O_5 600-nm-thick film at different C rates.

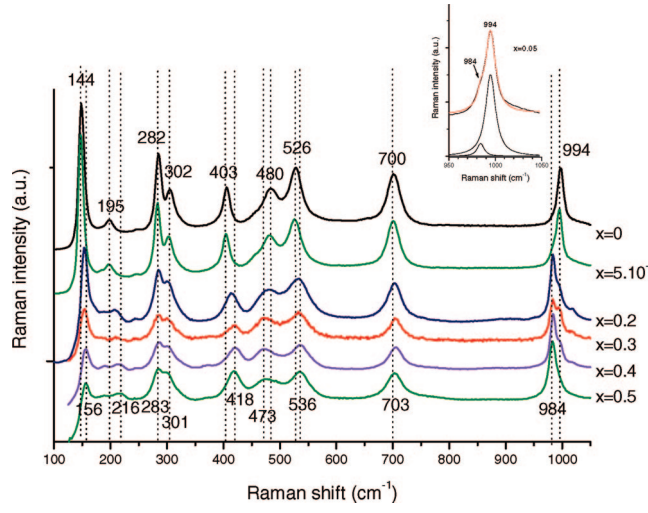

Figure 7. Raman spectra of a galvanostatically lithiated $Li_xV_2O_5$ thin film, $0 < x < 0.5$. An enlarged view of the high-frequency range for $x = 5 \times 10^{-2}$ is shown in the inset.

modes in the 200–700 cm^{-1} range are also shifted toward higher wavenumbers: 195 to 216 cm^{-1}, 403 to 418 cm^{-1}, 526 to 536 cm^{-1}, and 700 to 703 cm^{-1}. Conversely, the 480 cm^{-1} band shifts progressively to 473 cm^{-1} for $x = 0.5$. In the vanadyl stretching frequency range, we can see from the first lithium content value the appearance of a new component at 984 cm^{-1} which does not change in frequency but continuously increases in intensity at the expense of the 994 cm^{-1} band as x increases from 0.05 to 0.5. The Raman

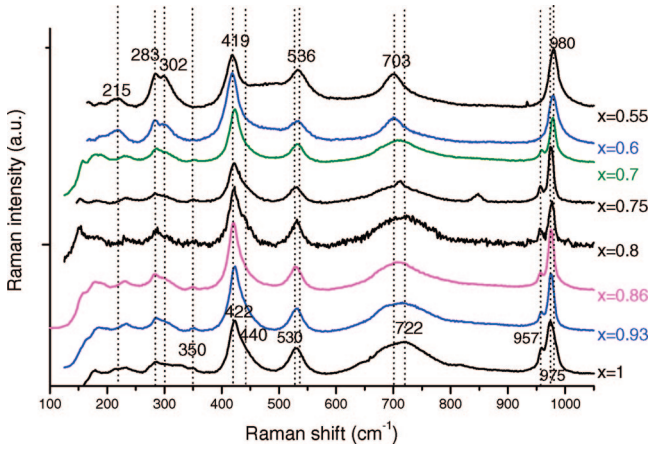

Figure 8. Raman spectra of a galvanostatically lithiated $Li_xV_2O_5$ thin film, $0.55 < x < 1$.

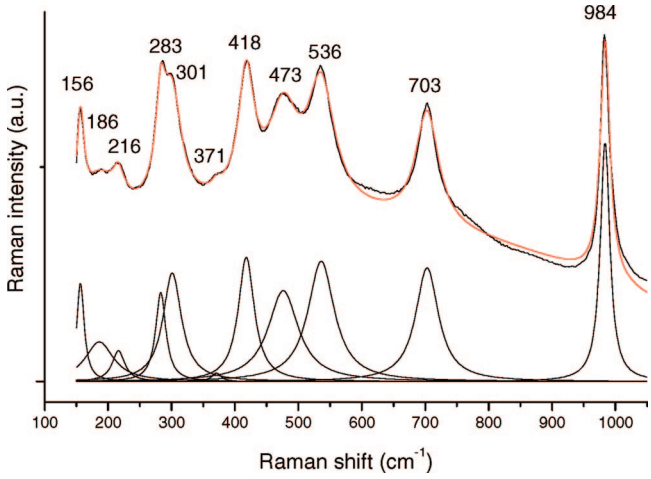

Figure 9. Raman spectrum of a galvanostatically lithiated $Li_{0.5}V_2O_5$ thin film, with the deconvolution of the different bands shown below.

spectrum of $Li_{0.5}V_2O_5$, reported in Figure 9, summarizes all of these changes.

For $0.5 < x < 1$ (Figure 8), in frequency ranges lower than 400 cm^{-1}, we observe a progressive loss of intensity, indicating a significant increase of the local disorder. Several bands progressively disappear, in particular, the low-frequency modes at 156 and 216 cm^{-1}, whereas the band at 473 cm^{-1} completely vanishes from $x = 0.5$ to $x = 0.55$. The 419 cm^{-1} band progressively shifts to 422 cm^{-1} for $x = 1$ and becomes asymmetric due to the emergence of a new component at 440 cm^{-1} from $x = 0.7$. The 536 cm^{-1} band progressively shifts to 530 cm^{-1}, whereas the 703 cm^{-1} line becomes broader and centered toward a higher wavenumber of 722 cm^{-1}. In the high wavenumber region (see enlarged view in Figure 10), the vanadyl stretching mode shifts toward a lower wavenumber, from 984 to 975 cm^{-1} in the lithium content range $0.5 < x < 0.7$, and then remains constant up to $x = 1$. For $x \geq 0.7$, several new Raman features are detected at 957, 681, 639, 350, and 440 cm^{-1}, as shown from the deconvolution reported in Figure 11 for the highest lithium uptake $x = 1$. The Raman spectrum of the LiV_2O_5 film is well consistent with that of the ϵ-rich powdered phase of LiV_2O_5 reported in ref 25.

Figure 12 shows the Raman wavenumber evolution as a function of the lithium composition in the $Li_xV_2O_5$ film for

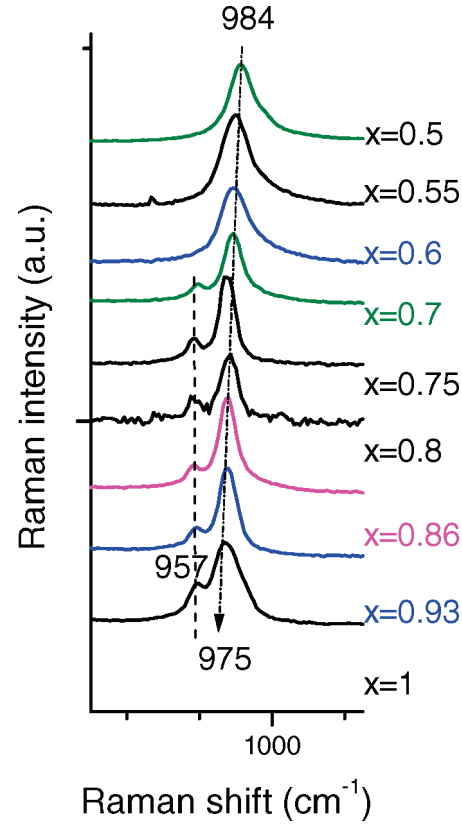

Figure 10. Enlarged view in the high-frequency range of the Raman spectra of a galvanostatically lithiated $Li_xV_2O_5$ thin film, $0.5 < x < 1$.

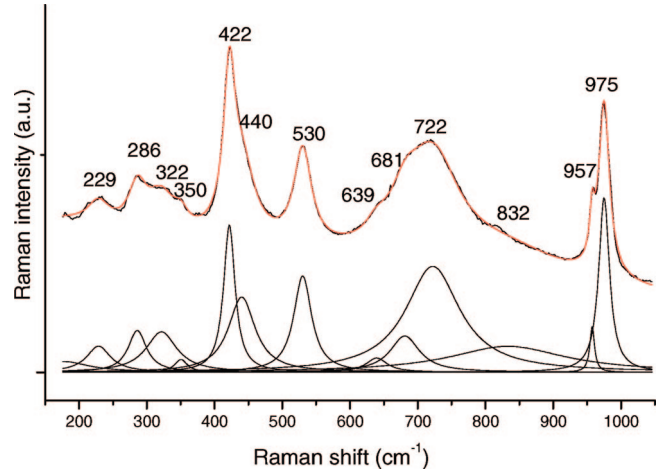

Figure 11. Raman spectrum of a galvanostatically lithiated LiV_2O_5 thin film, with the deconvolution of the different bands shown below.

the most prominent Raman bands located at 403, 526, 700, and 984 cm^{-1}. It is clear that two main domains of variation are observed.

For $x < 0.5$, the Raman spectra exhibit the same general features; in particular, the number of bands is kept. The observed intensity and frequency changes are directly related to the existence of a solid solution of Li in V_2O_5 corresponding to the ϵ-phase. They vary in a quite limited extent due to the similarity of the α- and ϵ-V_2O_5 related structures. Indeed, the Raman spectrum recorded for the $Li_{0.5}V_2O_5$ film (Figure 9) compares exactly with that previously reported for the chemically lithiated $\epsilon Li_{0.52}V_2O_5$ powder (Figure 13).[25] This finding is supported by the corresponding XRD data,

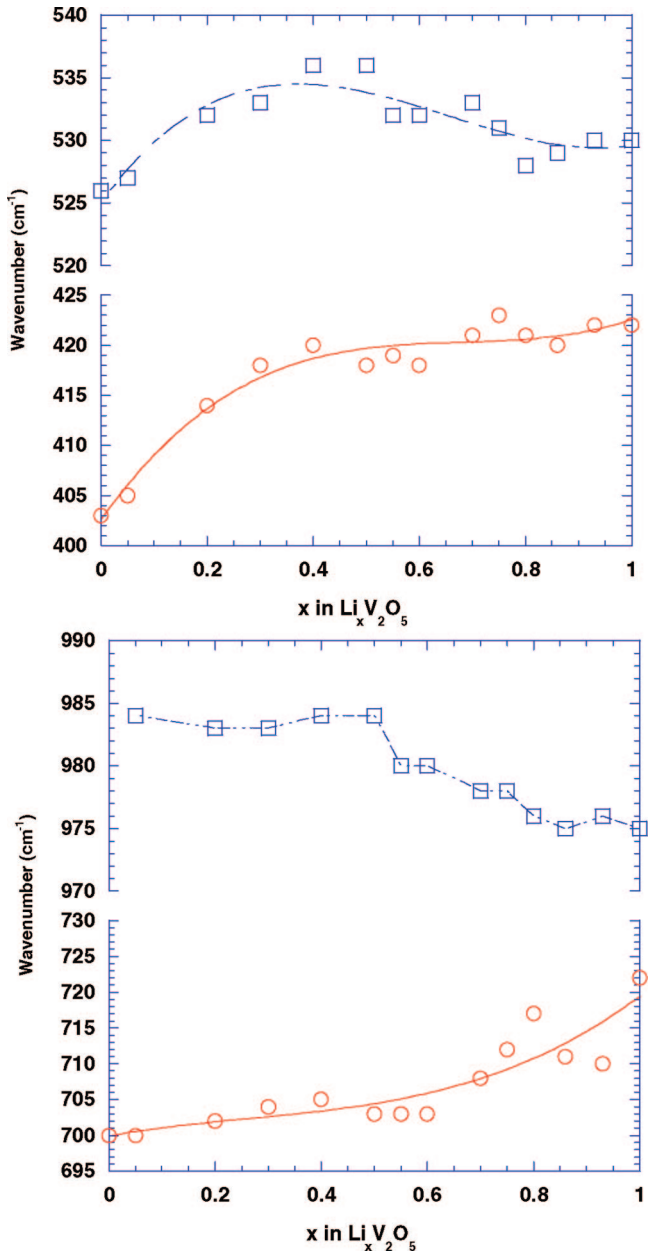

Figure 12. Evolution of the Raman band wavenumbers at 403, 526, 700, and 984 cm^{-1} as a function of x in the $Li_xV_2O_5$ thin film, $0 < x < 1$.

which clearly show a continuous increase of the c parameter and a correlated decrease of the a parameter.[15] The shift in frequency from 994 to 984 cm^{-1} for the apical $V-O_1$ stretching mode is consistent with the lengthening of the V═O bond from 1.58 Å for the α phase to 1.60 Å for the ϵ-$Li_{0.5}V_2O_5$ phase. Conversely, as shown in Figure 12, continuous displacements toward higher wavenumbers are observed when x increases up to 0.5 for the 403 and 526 cm^{-1} modes, which shift to 418 and 535 cm^{-1}, respectively. As these modes are all coming from oxygen displacements along the a axis, $x(O_1)$ and $x(O_{2'1})$, respectively, it is plausible that the stiffening of the lattice here observed can be related to the x dependence of the a parameter in the $Li_xV_2O_5$ film, which has been found to decrease from 11.51 to 11.35 Å when the lithium content increases from 0 to 0.55.[15] This result can be correlated to the existence of a compressive stress in V_2O_5 sputtered films evidenced by beam deflectometry[8] and varying in the same manner as the a parameter, that is, increasing upon lithiation in the $0 < x < 0.5$ domain. For $x > 0.6$, the relative stability of these $x(O_1)$- and $x(O_{2'1})$-related modes (see Figure 12) can be correlated with that of the a parameter.[15]

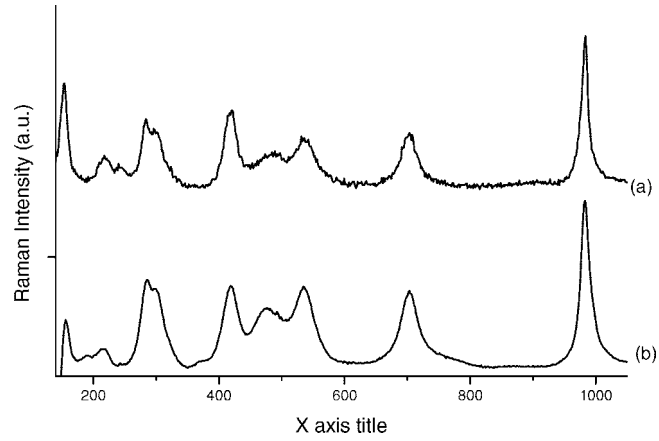

Figure 13. Raman spectra of (a) the chemical phase $\epsilon Li_{0.52}V_2O_5$[25] and (b) the $Li_{0.5}V_2O_5$ thin film.

For $0.5 < x < 1$, the spectral variations are less marked. The general features of the ϵ phase are kept. The continuous shift observed for the apical $V-O_1$ stretching mode from 985 to 975 cm^{-1} reflects a progressive weakening of the $V-O_1$ bond which is probably related to the linear expansion of the interlayer spacing observed for the ϵ phase, from 4.53 to 4.68 Å in the lithium composition range varying from 0.5 to 0.95.[15]

These results are consistent with XRD data,[8,9,13,15] which report that the structural response of such thin films consists of a solid solution behavior instead of the successive phase transitions usually described for the bulk material[16] and corresponding to the α, ϵ, and δ phases with the following compositions ranges, $0 \le x \le 0.15$, $0.3 \le x \le 0.7$, and $0.9 \le x \le 1$, respectively, separated by two-phase regions. It is clear that the Raman fingerprint of the ϵ phase appears here from the first lithium content value and is kept up to $x = 1$. At any moment, the characteristic Raman features of the δ phase are detected, in particular, the intense band at 1008 cm^{-1}.[25]

The spectral variations reported here are related to the local distortions occurring in the ϵ phase, which is able, in the thin film configuration, to accommodate up to 1 Li per mole of oxide. Although the lithium positions in the ϵ phase remain to be determined accurately, a unique type of lithium site has been described for the whole ϵ-phase domain. It consists of elongated cubo-octahedra joining common faces, the symmetry of such sites remaining unchanged with x.[29] However, it has been reported that increasing the amount of lithium in the ϵ phase leads to a lithium-rich phase (called ϵ') in which the lithium environment is modified:[29–31] for lithium amounts < 0.5, the number of unoccupied cubo-octahedra exceeds the number of occupied octahedra,

(29) Katzke, H.; Depmeier, W. *Phase Transitions* **1996**, *59*, 91.
(30) Rozier, P.; Savariault, J. M.; Galy, J.; Marichal, C.; Hirschinger, J.; Granger, P. *Eur. J. Solid State Inorg. Chem.* **1996**, *33*, 1.
(31) Savariault, J. M.; Rozier, P. *Physica B* **1997**, *234–236*, 97.

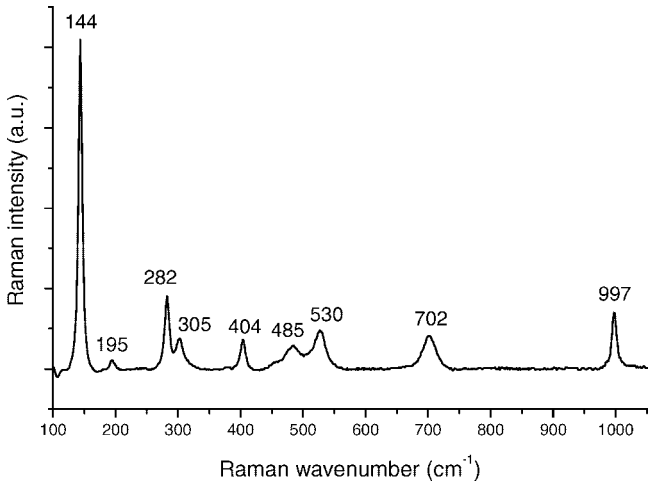

Figure 14. Raman spectrum of the reoxidized compound.

whereas above $x = 0.5$, neighboring cubo-octahedra have to be occupied. This causes a change in the interatomic Li−Li distances: the shortest Li−Li distance decreases from 7.2 Å for $x < 0.5$ to 3.6 Å for $x > 0.5$.[30] Hence, in contrast to the lithiated bulk material for which the $\epsilon \rightarrow \delta$ phase transition occurs from $x = 0.6$,[16] strong repulsive Li^+-Li^+ forces probably prevail in the film for the ϵ-rich phase but are allowed without giving rise to significant structural modification of the framework. This probably explains the Raman band splitting at 975 and 957 cm^{-1} as observed for the highest lithium uptakes ($x \geq 0.7$). The existence of these two stretching vanadyl modes may indicate the presence of two kinds of vanadium atoms. This can be explained by a change in electron localization for a higher depth of discharge.

The Raman spectrum of the reoxidized compound, reported in Figure 14, clearly exhibits the characteristic Raman features of the pure V_2O_5 lattice. The recovery of the structure is in good agreement with the excellent electrochemical reversibility evidenced in the 3.8/2.8 V potential range.

Previous Raman studies of lithium intercalated V_2O_5 films report scarce and contradictory results. Fast amorphization of the sputtered oxide has been observed in ref 21, the V_2O_5 lines vanishing nearly completely from the early lithium content values, whereas in ref 23, practically no change seems to take place in the pulsed laser deposition film in the $0 < x < 1$ composition range. Nevertheless, one should note that only two compositions ($x = 0.2$ and $x = 0.9$) are reported in ref 23, with their Raman spectra roughly assigned on the basis of the phase diagram described for the bulk material.

The present data obtained for sputtered thin films can be compared to those previously published by some of us for atomic layer deposition (ALD) thin films[22] and reconsidered in ref 25. For $x < 0.5$, the evolution of the Raman spectra is very close for both materials and reflects local distortions induced by Li accommodation into the ϵ phase. For $0.5 < x < 1$, only a shift of the vanadyl mode frequency from 980 to 970 cm^{-1} was observed for the ALD thin film. For $x = 1.1$, the Raman spectrum exhibited bands at 1004, 971, 957, 691, 528, 420, 347, 298, 282, 230, and 150 cm^{-1}, which are assigned to a mixture of the δ phase (band at 1004 cm^{-1}) and an ϵ-rich phase.[25] The difference in the structural response observed for $Li_xV_2O_5$ thin films in the $0.5 < x < 1$ composition range probably stems from an effect of the microstructure of the deposited films. Indeed, the as-deposited ALD films were amorphous and required a heat treatment at 400 °C for 48 h, leading to *00l*-oriented films and more crystallized deposits than our sputtered films. The broader XRD peaks of the present sputtered films[15] indicate smaller coherence domains, estimated to be on the order of 15 nm along the *c* axis.

Conclusion

Raman microspectrometry has been applied to investigate the local structure of sputtered V_2O_5thin films, 600-nm-thick, after electrochemical lithiation in the 2.8−3.8 V potential range. These films deposited on unheated stainless steel substrates and without any postannealing treatment exhibit a low crystallinity and a specific morphology corresponding to a *h00* preferred orientation. A qualitative characterization of the normal vibrations of the V_2O_5 lattice with their assignments to particular atomic displacements has allowed a discussion of the changes occurring in the Raman spectra of the $Li_xV_2O_5$ films for $0 < x < 1$. In particular, the vanadyl stretching mode located in the high wavenumber region (994 cm^{-1}) is of utmost importance since it constitutes a Raman band highly sensitive to Li interaction and then allows a meaningful and relevant discussion of experimental data. Three main results are obtained from the Raman features of the $Li_xV_2O_5$ films: (i) for $x < 0.5$, all the Raman bands are consistent with the existence of the ϵ phase, as confirmed by the Raman spectra of the electrochemical and chemical phases which completely superimpose with a vanadyl mode at 984 cm^{-1}. (ii) For $0.5 < x < 1$, a continuous shift mode from 984 to 975 cm^{-1} and the emergence of a new vanadyl band at 957 cm^{-1} from $x = 0.7$ have been ascribed to Li insertion into the ϵ phase with a continuous expanded interlayer distance. This finding is consistent with the occurrence of two kinds of Li sites reported in the literature for the Li-rich ϵ phase called ϵ'. (iii) The presence of the δ phase is never detected.

The experimental Raman data, in good accord with XRD results on the sputtered V_2O_5 thin film oxide, indicate the structural response of such films consists of a single phase behavior which strongly contrasts with the more pronounced structural changes described for bulk samples with the emergence of one- and two-phase domains as well as the formation of the δ phase from $x = 0.6$. It is thought that this difference mainly stems from a nanosize effect, the stacking of platelets occurring in our samples over only 10−20 nm. Hence, a more homogeneous Li insertion reaction can take place in the present films, then avoiding a local surlithiation phenomenon and allowing a better relaxation of the host lattice and a lower structural stress. Actually, the degree of crystallinity and the morphology of the thin films strongly contribute to the structural changes as Li accommodation proceeds.

CM702979K